Tailoring the Mechanical Properties of High-Aspect-Ratio Carbon Nanotube Arrays using a-SiC Coatings*

R.H. Poelma,[1] B. Morana,[1] S. Vollebregt,[1] E. Schlangen,[2]
H.W. van Zeijl,[1] X.J. Fan,[3] and G.Q. Zhang[1,†]

[1] *Department of Microelectronics, Delft University of Technology, Feldmannweg 17, 2628CT Delft, The Netherlands.*

[2] *Department Structural Engineering, Delft University of Technology, Stevinweg 1, 2628CN Delft, The Netherlands.*

[3] *Department of Mechanical Engineering, Lamar University, Beaumont, TX 77710, USA.*

(Dated: June 22, 2015)

Abstract

The porous nature of carbon nanotube (CNT) arrays allows for the unique opportunity to tailor their mechanical response by the infiltration and deposition of nano-scale conformal coatings. Here, we fabricate novel photo-lithographically defined CNT pillars that are conformally coated with amorphous silicon carbide (a-SiC) to strengthen the interlocking of individual CNTs at junctions using low pressure chemical vapour deposition (LPCVD). We further quantify the mechanical response by performing flat-punch nanoindentation measurements on coated CNT pillars with various high-aspect-ratios. We discovered new mechanical failure modes of coated CNT pillars, such as "bamboo" and brittle-like composite rupture as coating thickness increases. Furthermore, a significant increase in strength and modulus is achieved. For CNT pillars with high aspect ratio (1:10) and coating thickness of 21.4 nm, the compressive strength increases by an order of magnitude of 3, towards 1.8 GPa (from below 1 MPa for uncoated CNT pillars) and the elastic modulus increases towards 125 GPa. These results show that our coated CNT pillars, which can serve as vertical interconnects and 3D super-capacitors, can be transformed into robust high-aspect-ratio 3D-micro architectures with semiconductor device compatible processes.

Keywords: carbon nanotubes, nanoindentation, pillar compression, coating, failure

* Author correspondence

† http://www.tudelft.nl; G.Q.Zhang@tudelft.nl

I. INTRODUCTION

Vertically aligned carbon nanotube (CNT) arrays or forests in photo-lithographically defined patterns have been recognized as a promising structural material for the fabrication of high-aspect-ratio, three-dimensional (3D) micro- and nano-architectures [1–5]. The exceptional properties of CNTs and related materials have triggered tremendous efforts not only to study their intrinsic properties but also to explore their applications in a large variety of fields [6–13]. These high-aspect-ratio 3D structures play an important role in the advancement of vertical interconnect technology [14–17], flexible batteries [3], stamps for micro/nanoimprint lithography [2, 18–21], compliant thermal interface materials for low inter-facial resistances [22–25], 3D super-capacitors [26, 27] and nano/micro-electromechanical systems (NEMS) and (MEMS) [1, 28–30].

The CNT arrays that we refer to in this work are composed of nominally vertical, interwoven, multi-wall carbon nanotubes [31, 32]. A common procedure for growing high-aspect-ratio CNT arrays is via chemical vapor deposition (CVD) on photo-lithographically defined catalyst areas [5, 9]. One of the limitation of this growth process, is the low packing density of the CNTs inside the array [15, 33]. The interwoven CNTs inside the array are held together by a weak van der Waals interaction, allowing tubes to slide along each other [34, 35]. The combination of low packing density and weak inter-tube forces, results in mechanical properties of CNT arrays that are significantly inferior to individual CNTs [6, 35].

Consequently, a considerable amount of effort is going into the development of new methods to optimize the full potential of individual CNTs in low density CNT arrays, either by densification or application of conformal coatings. A literature overview of coated nanoscale architectures can be found in [36]. Recent and remarkable examples of conformally coated CNT arrays include *e.g.*, deposition of silicon coatings to create a flexible anode architecture for high-energy-density-batteries [3] and graphene coatings to create superelastic, lightweight and fatigue resistant aerogels [7].

Silicon carbide also proves to be an interesting coating material, mainly due to its diamond like characteristics [37]. The properties of SiC are especially attractive in applications which require contact, high temperatures, chemical inertness, high robustness, electrical conductivity and high resistance to electron beam damage [38–41]. Bulk composites containing SiC-coated CNTs have been produced by chemical vapour infiltration and were tested by

bending and a pull-out method. One remarkable result was the protection of CNTs from being oxidized at 1600 °C in air for 1 hour [42]. Investigations have also shown that SiC-coated multi-walled CNTs dispersed in composites increase fracture toughness and hardness [43].

The porosity of CNT arrays allows for infiltration and deposition of conformal coatings on individual CNTs inside the array. This results in the possibility to significantly alter the mechanical response of 3D-micro-architectures by changing the deposition thickness.

In this paper, we report the fabrication and testing of various high-aspect ratio pillars made from carbon nanotube arrays that are modified by thin conformal coatings of amorphous silicon carbide (a-SiC) deposited by low pressure chemical vapour deposition. We perform flat-punch nanoindentation measurements on CNT pillars to characterize the influence of conformal coatings of different thickness on the mechanical response of 3D-micro-architectures. We analyse the structural failure mode by performing scanning electron microscopy investigations after pillar compression. The specimens without coating show localized periodic buckling. Samples with thin coatings show bamboo-like failure while the samples with thick coatings show brittle ceramic failure. Furthermore, a significant increase of 3 orders of magnitude is measured for the compressive strength of pillars with a 21.4 nm thick coating of a-SiC.

II. DISCUSSION AND RESULTS

Carbon nanotube structures are grown by a common manufacturing process employing CVD on photo-lithographically defined catalyst areas (Supplementary A 1). After growth, the CNT arrays are conformally coated with 5.6 nm, 10.5 nm, 21.4 nm and 52.0 nm thin layers of amorphous silicon carbide (a-SiC) (Supplementary A 2). A matrix of as-grown CNT pillars with circular cross sections is shown in Fig. 1a. The pillars are (100 ± 2) µm tall and have lithographically defined diameters ranging from (5 ± 1) µm to (150 ± 1) µm. The maximum length to diameter L/D aspect ratio that results in highly vertical pillars is about 10:1. The morphology of the CNT pillars at 50, 100 and 150k magnification is shown in Fig. 1b, here it can be seen that individual CNTs inside the array are nominally vertical and interwoven. The low packing density is mainly caused by the relatively large spacing between catalyst particles which results in large spacing between individual CNTs

[33]. Examination of the CNT arrays at different stages; before and after coating, allows us to verify the coating process. Some single CNT fibres are bundled together into larger fibres due to the van der Waals attraction. The high magnification images in Fig. 1b, show a doubling of the fibre thickness with increasing deposition thickness, following the same trend as the measured film thicknesses of 5.6 nm, 10.5 nm, 21.4 nm and 52.0 nm of a-SiC on bare Si test wafers (Supplementary Fig. S2). The as-grown CNT array density is roughly $10^{10}\ tubes/cm^2$ which is determined from the SEM images of the pillars in Fig. 1b. The samples with a thick coating are still somewhat porous, this shows that precursor gases can still infiltrate the array and deposit a-SiC further inside the bundle.

To investigate the coating penetration depth and thickness we cleave several coated micropillars with a Berkovich nanoindentation tip. Afterwards, we use a Verios 460 extreme-high-resolution (XHR) SEM for characterization of the pillar cross-section (Supplementary A 2). The coating thickness reduces with roughly 0.14 nm per 1 µm surface penetration depth (Fig. S3). Closer inspection reveals that the CNTs, which are sticking out of the broken a-SiC matrix, have an average diameter of about 9 nm (Fig. S4). Furthermore, the high resolution SEM image shows that the coating thickness on the CNTs is in excellent agreement with the film thickness measured by ellipsometry on flat control samples.

A Raman spectrum analysis of the pillars is used to assess the quality of the CNTs before and after a-SiC deposition (Supplementary A 4). The data shows a convolution of the graphite (G) and disordered graphite (D) peaks together with the a-SiC peak into a single wide asymmetric peak near 1475 cm^{-1} (Supplementary Fig. S5). Deconvolution of the peaks using a least square fitting procedure shows that the intensity ratio I_G/I_D is reduced for thicker films of a-SiC. This indicates that the deposition of a-SiC might have reduced the quality of the CNTs. However, the scattering efficiency of amorphous carbon is relatively high when compared to graphite like carbon. The amorphous carbon would therefore yield a stronger Raman signal, which originates more from surface layers instead of the CNTs.

A. Compressive failure of uncoated CNT pillars

Uniaxial compression tests of micro- and nano-pillars using flat-punch nanoindentation offers a convenient method to effectively study their mechanical behaviour with high accuracy

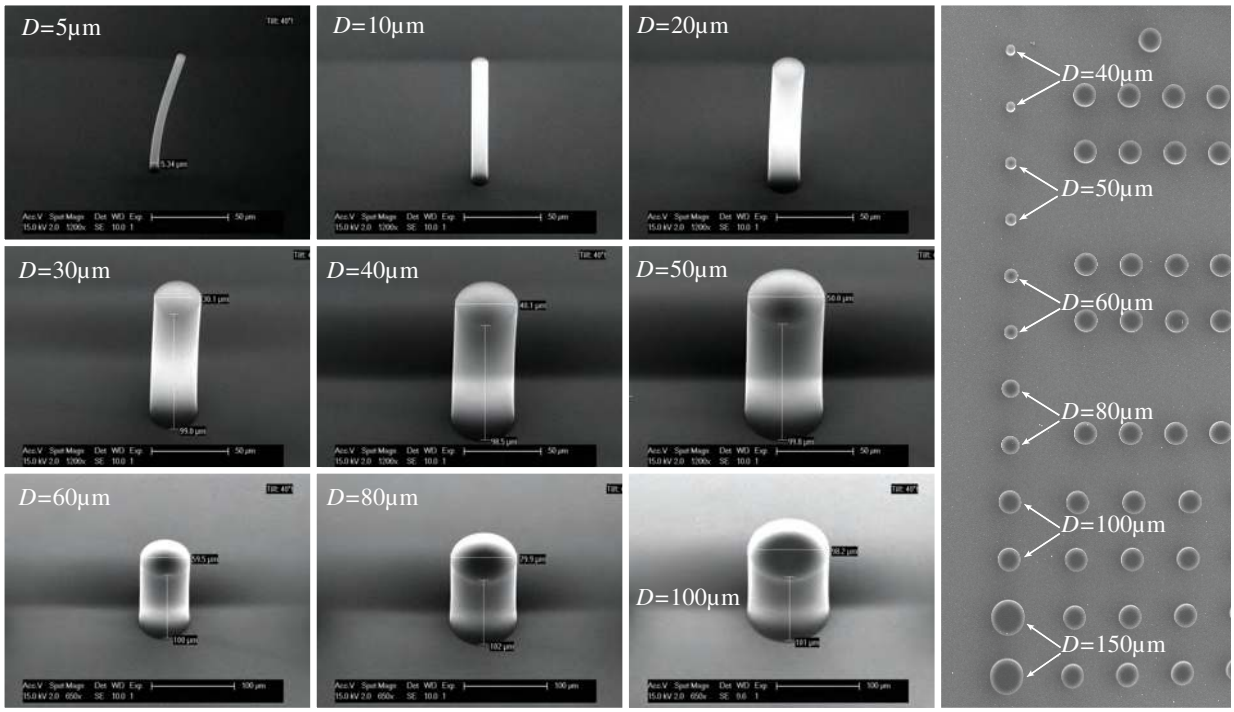

(a)

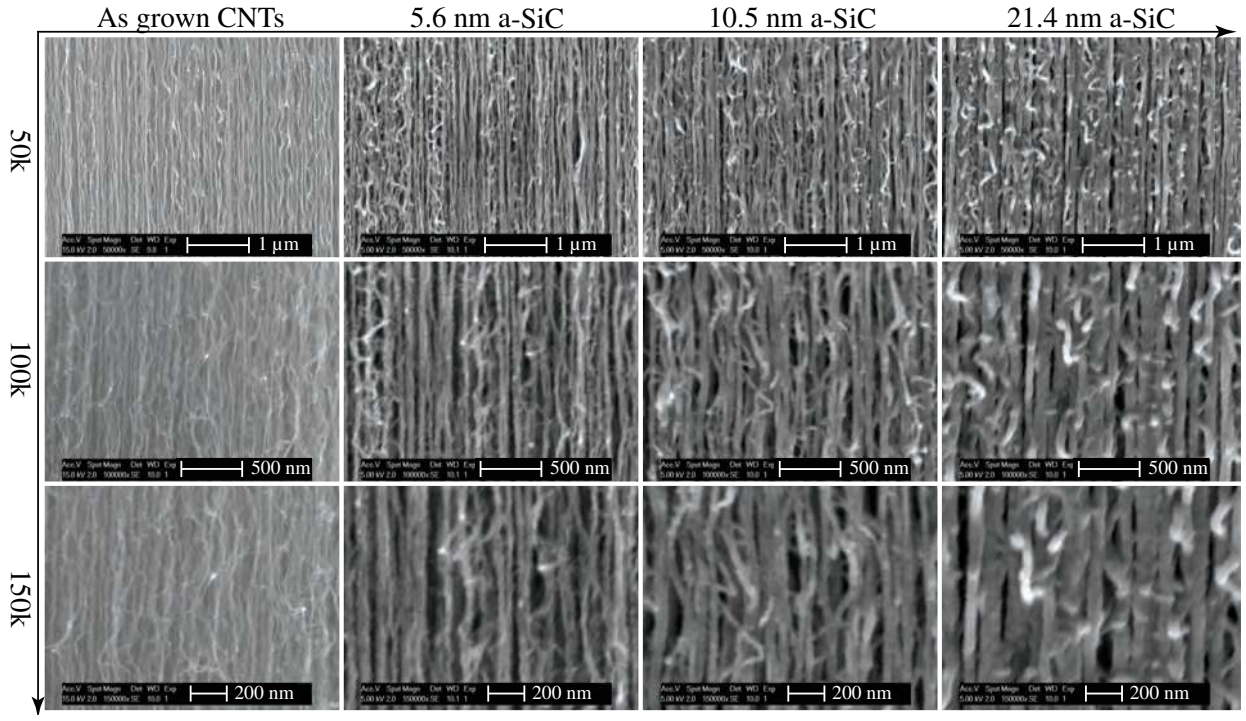

(b)

FIG. 1: Scanning electron microscopy images of (a) CNT pillars with varying aspect ratios on the left tilted views, on the right top view. (b) The morphology of the CNT pillar sidewall before and after a-SiC deposition at different magnifications.

and precision [44]. The mechanical response of our CNT pillars under uniaxial compression is characterized using nanoindentation with a custom-made flat-punch diamond indentation tip (Supplementary A 5). Scanning electron microscopy images of uncoated CNT pillars after compression reveal that the pillar failure mode is a type of localized periodic buckling which initiates at the base and propagates upwards throughout the entire bundle for increased compression depth, see Fig. 2a. The top three pillars with 100, 80 and 60 µm diameters were compressed 25, 20 and 17 % respectively and show 1 or 2 buckling-wavenumbers. The bottom three pillars with 50, 40 and 30 µm diameters were compressed 80% and show wavenumbers in the range of 9 to 11. These typical buckling characteristics appear to be unique for uncoated CNT arrays. More importantly, the localized periodic buckling events are very reproducible and in excellent agreement with the in-situ CNT array compression observations from *Shelby* and *Maschman et. al.* [5, 9]. Their observations also indicate that buckling events originate at the base of the pillar and the buckling wave-number increases with increasing compression depth of the pillars. The load-displacement and stress-strain response up until failure of uncoated CNT pillars are shown in Fig. 2b and Fig. 2c respectively. Multiple measurements on different pillars with a 100 µm diameter show a high degree of repeatability. Measurement on a 60 µm diameter pillar show that the stress increases monotonically for increasing compression, see regime (I) in Fig. 2c. The maximum stress that can be applied before the pillar collapses is about 0.85 MPa at a critical compressive strain of about 4.8%. When this stress is exceeded the system transitions from a stable regime (I) towards an unstable regime (II) with rapid strain bursts. The large distance between the line markers indicates buckling or structural collapse of the pillar which results in an overshoot of the nano-indentation tip towards the substrate. The displacement control of the nano-indenter-equipment is not fast enough to capture the fast decrease in load when the specimen fails. In the final unloading regime it is shown that the pillars remain permanently deformed with little strain recovery $\epsilon_r \leq 2\%$. The volume shrinkage after buckling is therefore about equal to the amount of compression and can be as high as 60% to 80%, see Fig. 2a. Uncoated pillars with diameters below 60 µm proved to be too challenging to measure due to adhesion of the pillars to the indentation tip and are therefore omitted from the results.

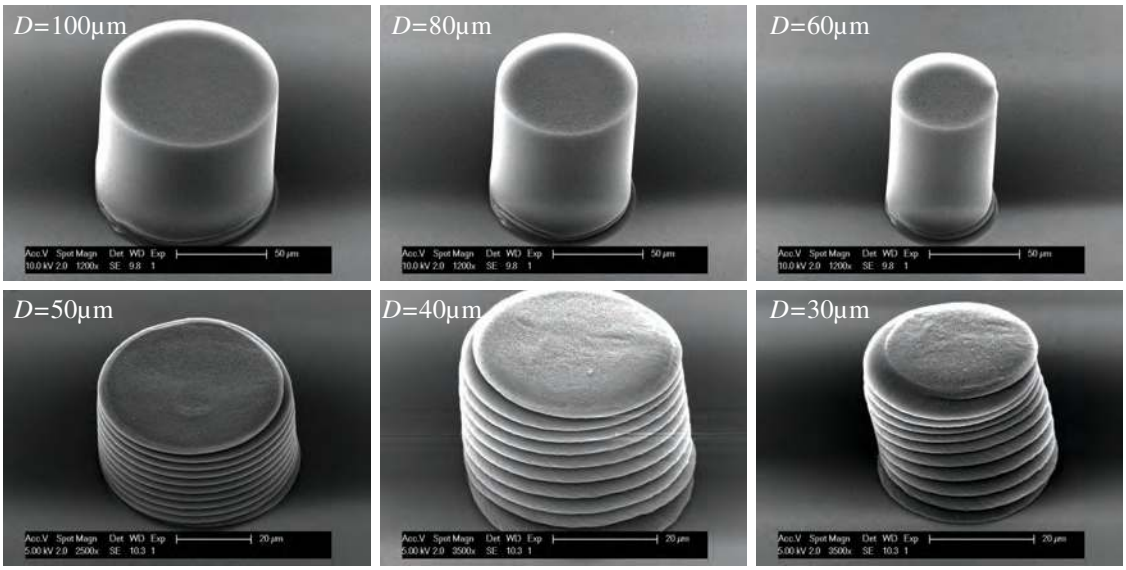

(a)

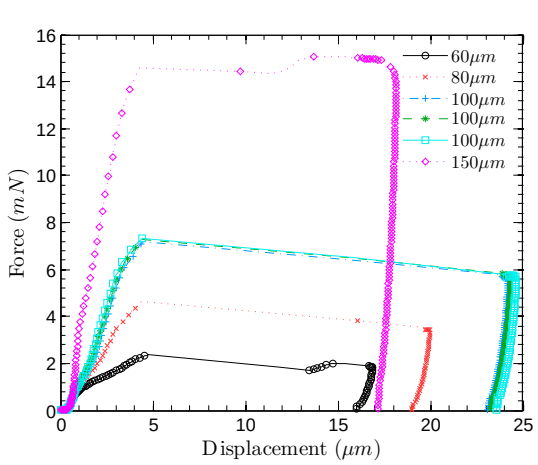

(b)

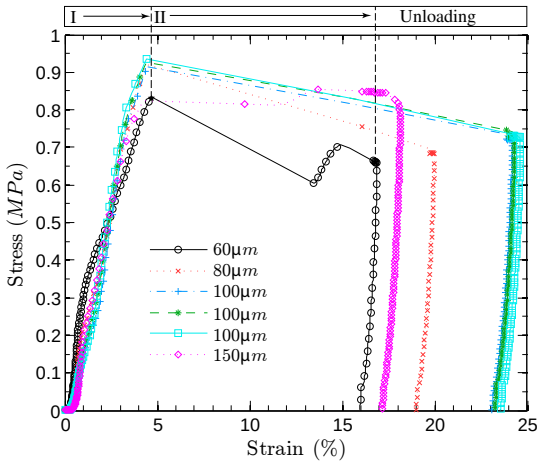

(c)

FIG. 2: Mechanical response of uncoated CNT pillars. (a) SEM images showing the compressive failure of uncoated CNT pillars of different diameters. The top row was compressed 20 µm, the smaller diameter pillars were compressed 80 µm. (b) The measured load versus displacement and (c) the engineering stress versus strain response.

B. Compressive failure of coated CNT pillars

An exciting observation can be made from the post compression morphology of pillars with a 5.6 nm thin conformal coating of a-SiC, see Fig. 3a. We see highly aligned vertical cracks and barely visible wrinkles on the outer surface which have originated from localized

buckling and kinking of the CNT fibres. Furthermore, the failure does not initiate from the base and the distinctive periodic buckling which appeared in uncoated pillars, is no longer observed.

The results indicate composite failure in the form of matrix or matrix - CNT interface failure. From a cylindrical perspective, vertical cracks are induced when the circumferential stress at the exterior of the pillar exceeds the composite strength. Circumferential stress is strongly dependent on radius and internal pressure. During compression, the pillar internal pressure might increase due to internal localized periodic buckling events that exert pressure on the surrounding material. As a consequence, a strong diameter dependency is observed in the compressive strength of the coated pillars. The mechanism is then crack propagation inside the matrix parallel to the fibre (CNT) orientation. This leads to gradual crushing and a distinct splitting shape of failed pillars resembling bamboo under uniaxial compressive loads [45, 46].

When compared to the uncoated CNT pillars, the mechanical behaviour changed from a foam-like material, where the dominant failure mode is localized periodic buckling, towards a bamboo-like failure similar to typical fibre reinforced composites. The accompanying stress versus strain response of the coated pillars see Fig. 3c, show an increase in compressive strength and a strong diameter dependency, where the small 20 µm diameter pillars have higher compressive strengths of about 12 MPa. Three distinct regimes can be identified; regime (I) ($0\% \leq \epsilon \leq 2\%$) elastic deformation, regime (II) ($2\% \leq \epsilon \leq 5\%$) small strain burst propagation, while regime (III) ($\epsilon > 5\%$) shows large strain burst propagation. The regimes (I), (II) and (III) have been illustrated in Fig. 3c for a 100 µm diameter pillar. The compressive strength of the pillars is defined as the maximum stress that can be applied before transition occurs from regime (I) to (II). We think that regime (II) can be attributed to non-periodic local buckling while regime (III) is composite failure and splitting of the bundle.

Furthermore, a significant recovery ($\sim 70\%$) of all deformed pillars towards their original position occurs during unloading even though cracks have appeared. The attraction between CNTs becomes more prominent as they come in closer proximity during compression, which can result in sticking and therefore low recovery of uncoated CNT arrays [47]. This suggests that during compression of the samples with 5.6 nm a-SiC coating, the elastic energy stored inside the coated CNTs is enough to overcome the attractive van der Waals

force. At the same time the coating is thin enough to allow for a certain degree of flexibility before fracturing. Moreover, the coating interlocks and constrains most of the interwoven CNTs at their junctions. Thus, preventing the tubes from sliding and rotating along each other by replacing the relatively weak van der Waals interaction with a solid cohesive bond and therefore preventing energy dissipation. We hypothesize that these effects combined, attribute to an improved strain recovery of the coated CNT array.

Post compression inspection of samples with thicker coatings of 10.5 nm and 21.4 nm of a-SiC, reveal a more destructive failure, see Fig. 4 and Fig. 5 respectively. This can be related to a more dominant brittle failure mode of the a-SiC matrix when the coating thickness is increased. Furthermore, a type of kink banding failure is initiated at the base of the pillar at a similar location as the localized buckling events in uncoated samples. In addition, CNT fibre fracture is observed after compressive failure. The stress strain curves Fig. 6b and Fig. 6d confirm brittle failure due to the almost instantaneous transition from the elastic regime towards structural collapse without yielding, strain bursts or localized buckling events. Finally we tested samples with a coating thickness of 52.0 nm of a-SiC. The pillars were too strong and could not be damaged due to the maximum load limitations of the nanoindentation equipment, see Fig. 6e and Fig. 6f. With the use of a Berkovich tip the pillars were finally destroyed, see Fig. S8. Due to the very strong pillar and violent destruction, the fracture propagated from the pillar into the bulk Si substrate.

The compressive strength of CNT pillars with different coating thickness has been examined. Their strength is defined as the maximum stress that can be applied before initiation of strain bursts, buckling or structural collapse occurs. This corresponds with the transition of regime (I) towards regime (II). Fig. 7 displays an overview of the maximum compressive stress of high-aspect ratio coated and uncoated CNT pillars. A high degree of repeatability is found for measurements on different pillars with a 100 µm diameter, each average is composed of about 12 measurements. For the smaller diameter pillars the average is composed of 1 to 4 measurements, since these pillars are fewer in number. The compressive stress increases with thicker coatings and for decreasing pillar diameter. A relatively high compressive strength (800 MPa to 1.8 GPa) is achieved for high-aspect ratio pillars ($L/D > 100 : 30$) with 21.4 nm thick coatings of a-SiC. The significant increase in compressive stress is about 3 orders of magnitude higher than uncoated pillars. It shows that careful control of nanometre thin conformal coatings of a-SiC can increase the strength of CNT array micro-structures

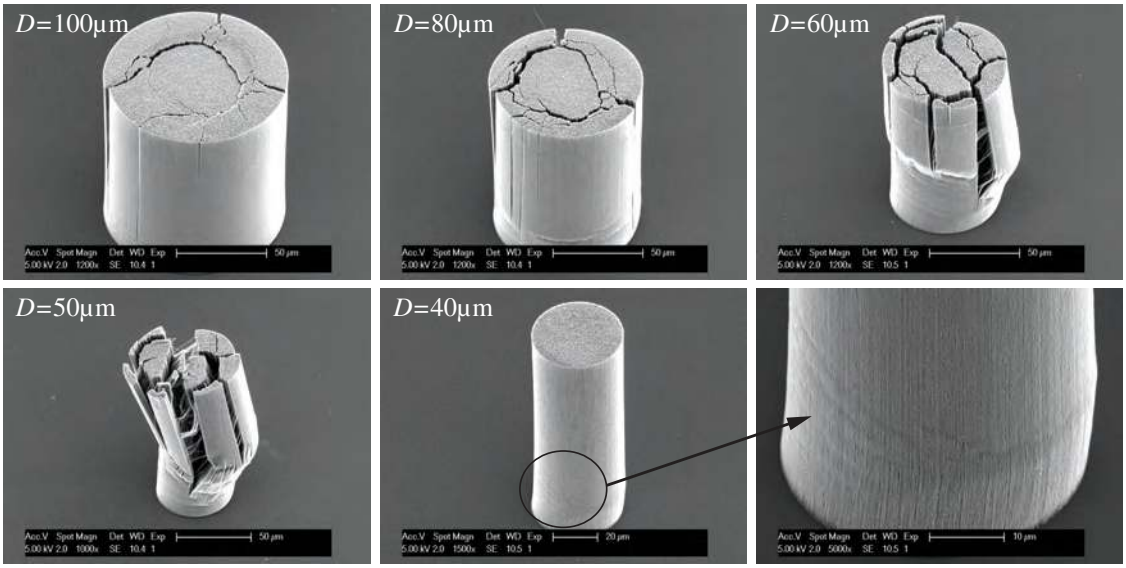

(a)

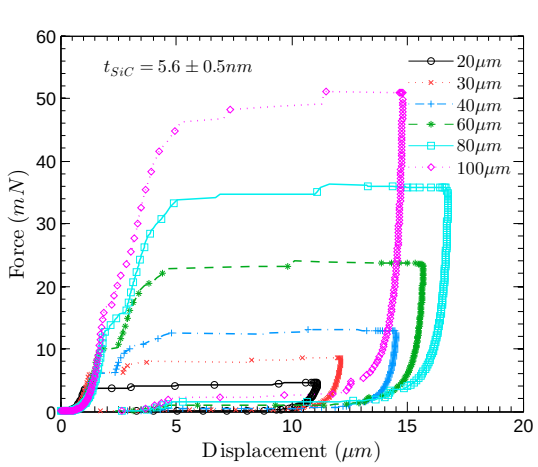

(b)

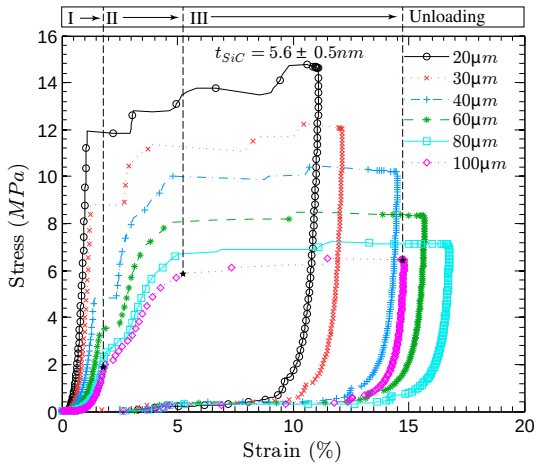

(c)

FIG. 3: Mechanical response of CNT pillars with a 5.6 nm thick a-SiC coating. (a) SEM images showing the compressive failure of coated CNT pillars of different diameters. (b) The measured load versus displacement and (c) the engineering stress versus strain response.

by several orders of magnitude.

For the uncoated pillars, owing to the low density and waviness of the long and slender CNTs inside the array, it is expected that they mostly carry bending and torsional forces instead of normal forces. This draws a strong resemblance with open-cell foams [48, 49]. When a conformal coating of 21.4 nm is applied to the CNTs, the porosity of the array is re-

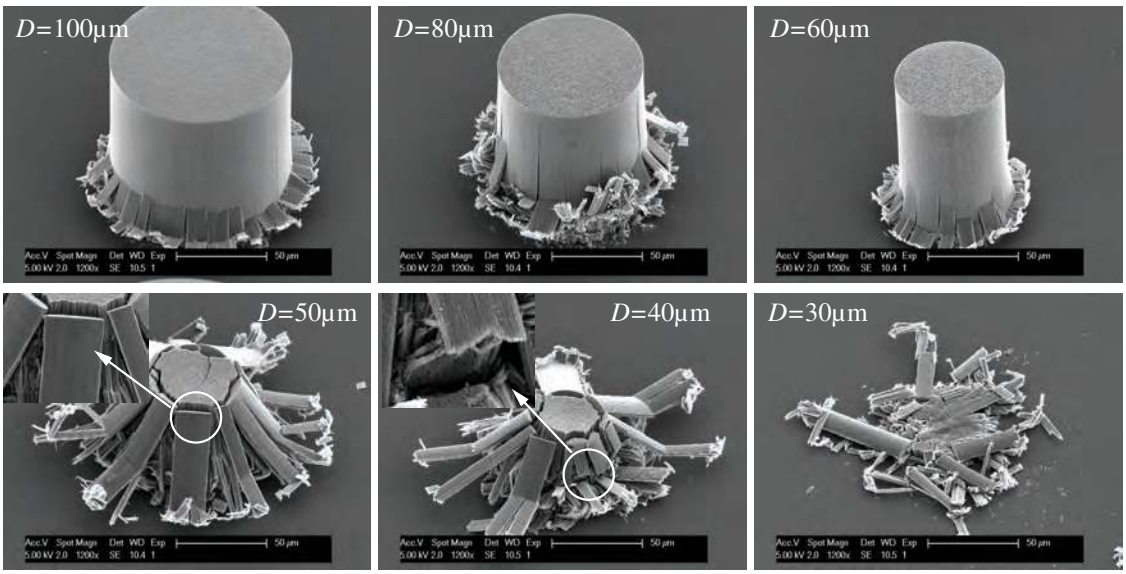

FIG. 4: Compressive failure of CNT pillars coated with 10.5 *nm* a-SiC.

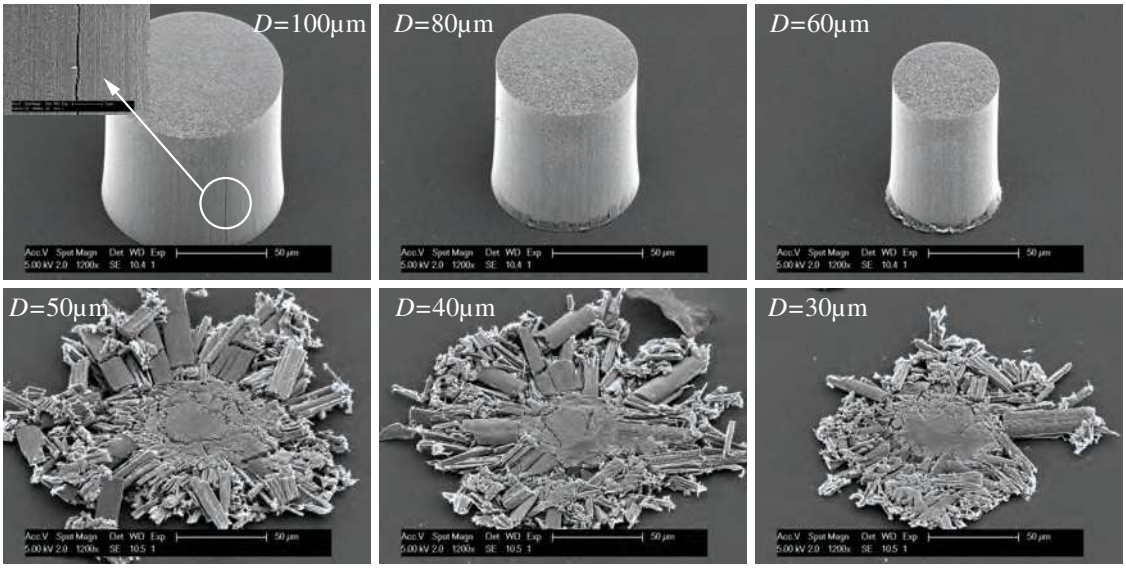

FIG. 5: Compressive failure of CNT pillars coated with 21.4 *nm* a-SiC.

duced from roughly 99% to 79% (Supplementary A 3) and the bending stiffness of the highly flexible CNTs inside the pillar is increased. Moreover, the contribution from normal forces or stiffness originating from CNT fiber extension and compression becomes more significant as coating thickness increases. The coating interlocks and constrains the interwoven CNTs at their junctions. With a thicker coating, a larger distance between the CNTs can be bridged, subsequently bonding more CNTs together and reducing the porosity. As a consequence, the mechanical response of coated CNT arrays changes from foam-like, towards bamboo-like

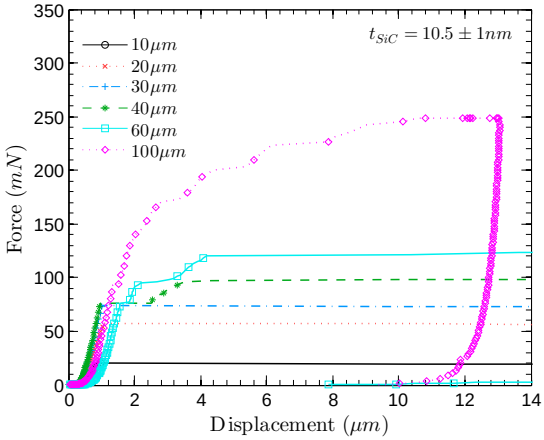

(a) 10.5 nm thick a-SiC coating.

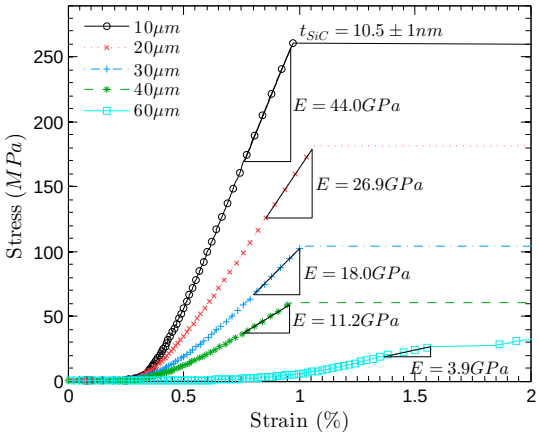

(b) 10.5 nm thick a-SiC coating.

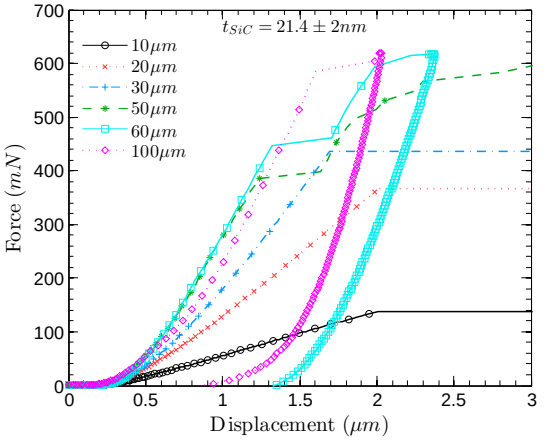

(c) 21.4 nm thick a-SiC coating.

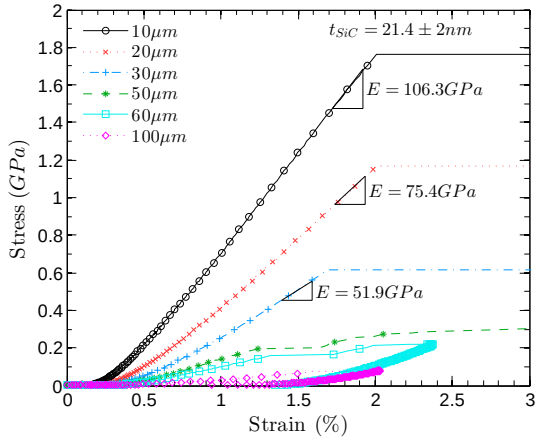

(d) 21.4 nm thick a-SiC coating.

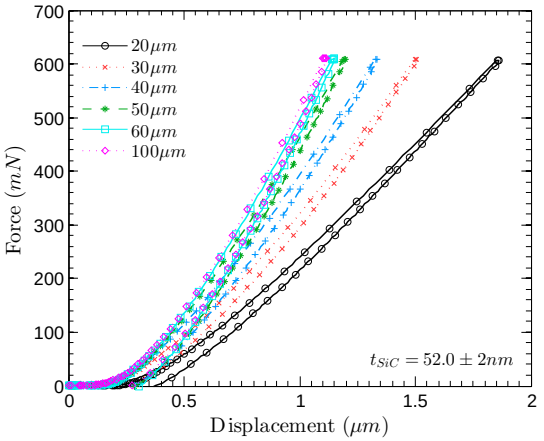

(e) 52.0 nm thick a-SiC coating.

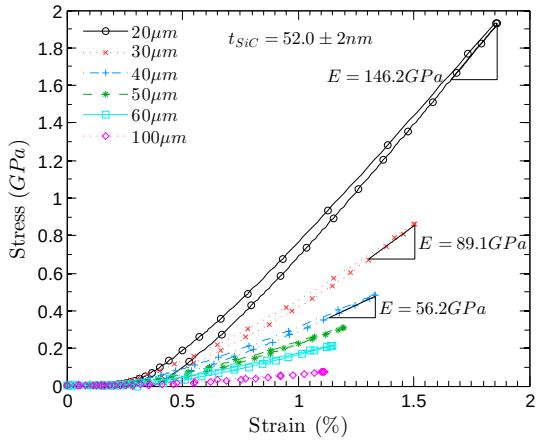

(f) 52.0 nm thick a-SiC coating.

FIG. 6: Mechanical response of CNT pillars with a 10.5 nm, 21.4 nm and a 52.0 nm thick a-SiC coating. (a,c,e) The measured load versus displacement and (b,d,f) the engineering stress versus strain response.

and finally brittle-ceramic-like as coating thickness increases. A coating thickness gradient will cause the effective mechanical material properties of the pillar to strongly increase in radial direction from the centre. Thus, explaining the diameter dependency of the material properties of the coated pillars and drawing additional similarities with other types of orthotropic materials such as wood or bamboo.

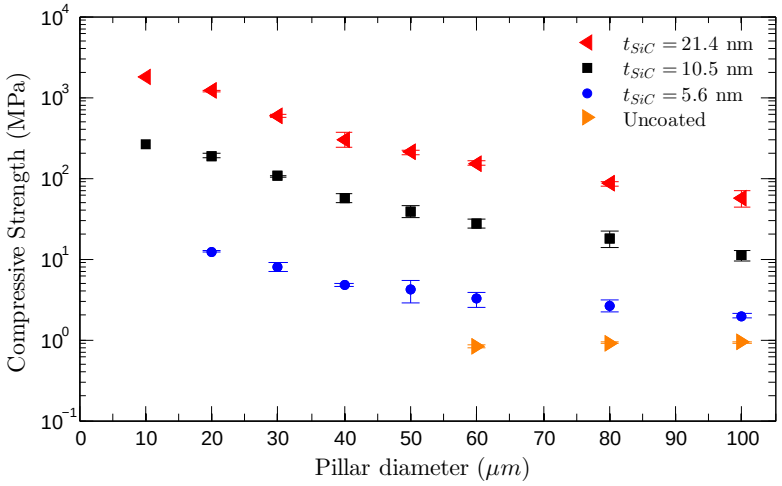

FIG. 7: Compressive failure stress of coated and uncoated pillars.

C. Young's modulus

The effects of thin conformal a-SiC coatings on E the Young's modulus of CNT pillars are measured using the continues stiffness measurement (CSM) mode of the nanoindenter (Supplementary Fig. A 5). The uncoated samples and those with a thin a-SiC coating of 5.6 nm have all collapsed before a plateau region was reached (Fig. S7a and Fig. S7b). The effective Young's modulus of coated pillars increases drastically with increasing coating thickness. We find that the Young's modulus increases with compression depth and plateau regions are observed for samples with 10.5 and 21.4 nm thick a-SiC coatings. The measured moduli in Fig. S7 are in excellent agreement with the moduli extracted from the slope of the stress-strain curves before failure occurs, see Fig. 6b and Fig. 6d, respectively. Another observation shows that E increases for coated pillars of smaller diameter, following the same trend as the compressive strength Fig. 7. A gradient in the coating thickness as a function of the surface penetration depth can be a possible explanation for the observed

pillar diameter dependency of the compressive strength and Young's modulus measurements, Supplementary A 2 gives a more in depth analysis.

III. CONCLUSIONS

Carbon nanotube pillars were grown and their mechanical response was modified from foam like towards brittle ceramic behavior, using a straightforward process of depositing nanoscale conformal coatings of amorphous silicon carbide (a-SiC) by low pressure chemical vapor deposition. The failure mode of coated pillars was characterized using nanoindentation with a flat cylindrical punch. The dominant failure mode changed from localized periodic buckling towards bamboo-like failure and finally towards brittle ceramic failure as coating thickness increased. Vertical cracks at the exterior of the pillar were induced when the circumferential stress exceeded the composite strength during compression. We conclude that conformal coatings reduce the porosity of the array and increase the stiffness of the highly flexible CNTs. Furthermore, the connections between neighboring tubes inside the CNT array are increased and changed from weak van der Waals interaction for the uncoated arrays, towards a bonded a-SiC connection.

As a result, a tremendous increase of 3 orders of magnitude for the Young's modulus and compressive strength of pillars with a 21.4 nm thick deposition of a-SiC was achieved. The Young's moduli increased from 200 MPa for uncoated pillars at 1 µm compression depth towards a high value of about 125 GPa for a 10 µm diameter pillar with a thin conformal coating of 21.4 nm a-SiC. Furthermore, the compressive strength of uncoated pillars increased from values below 1 MPa towards a maximum of 1.8 GPa. We therefore propose that the fast growing, conformal coated, CNT arrays can be useful as a strong structural material for creating robust high aspect ratio 3D-micro architectures.

IV. EXPERIMENTAL SECTION

CNT Growth: The first step in the synthesis of different aspect-ratio CNT pillars consists of growing a 170 nm thick thermal silicon oxide layer on a silicon wafer substrate to prevent diffusion of the metal catalyst into the substrate. Next, a 15 nm thin layer of alumina (Al_2O_3) is sputtered on the substrate to increase the CNT nucleation density from the catalyst

particles [50]. For the lift-off process we spin coat and pattern, using optical lithography, a film of 1.5 µm thick negative photo-resist (AZ Nlof2000). Then a 2 nm thin layer of iron (Fe) catalyst is deposited on the Al_2O_3 film by electron beam evaporation. The catalyst is patterned by a lift-off process using a NMP (C_5H_9NO) solvent at 70 °C for dissolving the resist. Next, (100 ± 2) µm tall vertically aligned multi-wall CNTs are grown in 5 minutes by low pressure chemical vapour deposition (LPCVD) in a commercial deposition system (Black Magic Pro, Aixtron). The CNTs are grown at a temperature of 600 °C using a gas flow mixture of 700 sccm hydrogen over 50 sccm acetylene (H_2/C_2H_2) at 80 mbar.

Conformal Coating: The a-SiC films are deposited inside a Tempress hot-wall LPCVD furnace using dichlorosilane (SiH_2Cl_2) and acetylene (C_2H_2) as gas precursor diluted at 5% in hydrogen (H_2). The deposition temperature and pressure are set to 760 °C and 1 mbar, respectively. The gas flow rates are 65 sccm SiH_2Cl_2 over 435 sccm C_2H_2 in 5% H_2. A detailed description of different SiC deposition process recipes and their characterization is described in previous work [38].

Mechanical Characterization: The mechanical response of CNT pillars is characterized using nanoindentation with an Agilent MTS Nanoindenter XP G200. Uniaxial compression of the CNT pillars was achieved by using a 150 µm diameter custom made flat-punch diamond indenter tip. For each test we detect the surface on a neighbouring pillar to avoid affecting the pillar on which measurements are performed. Force, displacement and stiffness data were acquired using the continuous stiffness measurement (CSM) technique. The CSM settings used are: 2 nm amplitude, 45 Hz frequency, sensitive 100 N m^{-1} surface detection and a strain rate of 0.01 s^{-1}.

SUPPORTING INFORMATION

Supporting Information is available from the Wiley Online Library or from the author.

ACKNOWLEDGMENTS

We wish to acknowledge the support of the DIMES Technology Centre for their assistance during the clean room processing, I.G.C. Weppelman and C.Th.H. Heerkens from the Charged Particle Optics group for the Verios 460 extreme-high-resolution (XHR) SEM

support.

Appendix A: Supporting Information

1. CNT sample preparation

The synthesis of different aspect-ratio CNT pillars is illustrated in Fig. S1a. The first step consists of growing a 170 nm thick thermal silicon oxide layer on a silicon wafer substrate to prevent diffusion of the metal catalyst into the substrate. Next, a 15 nm thin layer of alumina (Al_2O_3) is sputtered on the substrate to increase the CNT nucleation density from the catalyst particles [50]. Then a 2 nm thin layer of iron (Fe) catalyst is deposited on the Al_2O_3 film by electron beam evaporation. The catalyst is patterned using optical lithography and a lift-off process Fig. S1b. For the lift-off process we spin coat a film of 1.5 µm thick negative photo-resist (AZ Nlof2000) and use a NMP (C_5H_9NO) solvent at 70 °C for dissolving the resist during the lift-off. Next, (100 ± 2) µm tall vertically aligned multi-wall CNTs are grown in 5 minutes by low pressure chemical vapour deposition (LPCVD) in a commercial deposition system (Black Magic Pro, Aixtron) (Fig. S1c). The CNTs are grown at a temperature of 600 °C using a gas flow mixture of 700 sccm hydrogen over 50 sccm acetylene (H_2/C_2H_2) at 80 mbar.

2. CNT coating procedure

The CNT arrays are conformally coated with a-SiC to promote the interlocking of individual CNTs at junctions, see Fig. S1d. Low pressure chemical vapour deposition (LPCVD) allows for controlled deposition of very thin and conformal layers. The deposition parameters; temperature and ratio of precursor flows, were tuned in order to obtain amorphous layers of silicon carbide (a-SiC). The slow rate of deposition of a-SiC improves the infiltration of the precursor gases inside the porous CNT array. Poly-SiC layers have a higher deposition rate and they tend to close the CNT array on the outer surface before complete infiltration occurs. Hence, a-SiC deposition results in a more conformal layer deposited on the CNTs.

The a-SiC films are deposited inside a Tempress hot-wall LPCVD furnace using dichlorosilane (SiH_2Cl_2) and acetylene (C_2H_2) as gas precursor diluted at 5% in hydrogen (H_2). The deposition temperature and pressure are set to 760 °C and 1 mbar, respectively.The gas flow

rates are 65 sccm SiH_2Cl_2 over 435 sccm C_2H_2 in 5% H_2. A detailed description of different SiC deposition process recipes and their characterization is described in previous work [38].

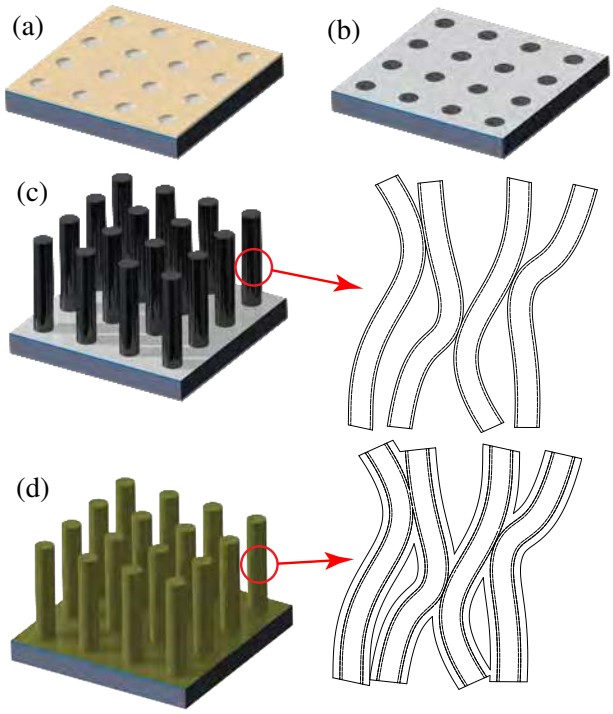

FIG. S1: Schematic illustration of the fabrication procedure. (a) Si substrate with thermal SiO_2, sputtered Al_2O_3 and patterned photo-resist. (b) E-beam evaporation of Fe and lift-off procedure. (c) CNT growth and microstructure illustration. (d) Conformal amorphous-silicon carbide coating and the modified array microstructure.

The a-SiC layer thickness is controlled by careful timing of the deposition process. Bare silicon test wafers are added to the processing batch as reference. The layers are measured by variable angle spectroscopic ellipsometry using a Woollam M-2000UI® ellipsometer. The spectra are obtained at 7 different angles between 45° and 75°, in the spectral range of 245 nm and 1690 nm. The reference measurement on bare Si wafers is used as an estimation of the deposited a-SiC thickness on the CNTs. The deposition times that correspond with a film thickness of 5.6 nm, 10.5 nm, 21.4 nm and 52.0 nm is respectively 18 min, 28 min, 50 min and 120 min, see Fig. S2. From the linear fit we estimate a deposition rate of about 5 Å min^{-1}. Furthermore, we have confirmed t_{inc}, an incubation time of about 7 min before the films starts growing. It should be noted that the incubation time and therefore the final thickness of a-SiC on CNTs might be different than a-SiC on bare silicon test wafers due to

the difference in substrate material. In addition, the porous CNT pillars have a large surface area to volume ratio. The gas precursors in LPCVD react with the surface they come into contact with. Therefore, the concentration of precursor reactants inside the CNT array can reduce when the gas infiltrates the CNT pillar further. Consequently, this might lead to a reduction of the deposition rate of a-SiC inside the bundle. As a result, pillars with larger diameters can have a thinner layer of a-SiC deposited on the inside of the pillar than on the outside.

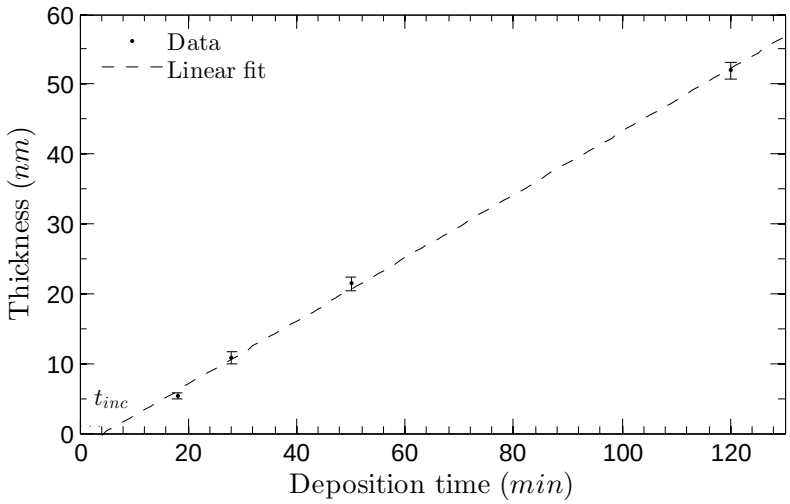

FIG. S2: Ellipsometer measurements of the LPCVD a-SiC film thickness on bare silicon test wafers versus deposition time. The dots are the measured data the broken line represent the expected values generated from a linear fit. The data suggests the presence of an incubation time t_{inc} before the films starts growing in thickness.

The coating penetration depth and thickness is investigated by splitting the 10.5 nm a-SiC coated micropillars with a Berkovich tip, see Fig. S3a-b. A Verios 460 extreme-high-resolution (XHR) SEM is used to perform an investigation on the coating inside the pillar. The first observation is that the coating appears to penetrate the bundle fully, however the coating thickness decreases for increased penetration depth. The coated CNT bundles near the outer surface of the pillar have an average diameter of about 30 nm (Fig. S3d), the uncoated CNTs have an average diameter of about 9 nm (Fig. S4). Therefore the coating thickness t_{SiC} on the CNTs is about 10.5 nm which is in excellent agreement with the film thickness measured by ellipsometry on bare Si test wafers. Moving 20 µm deeper inside the pillar, we notice that the average coating thickness is reduced to about 6.5 nm (Fig. S3e).

At 40 µm penetration depth, the coating thickness is reduced to about 5 nm (Fig. S3f).

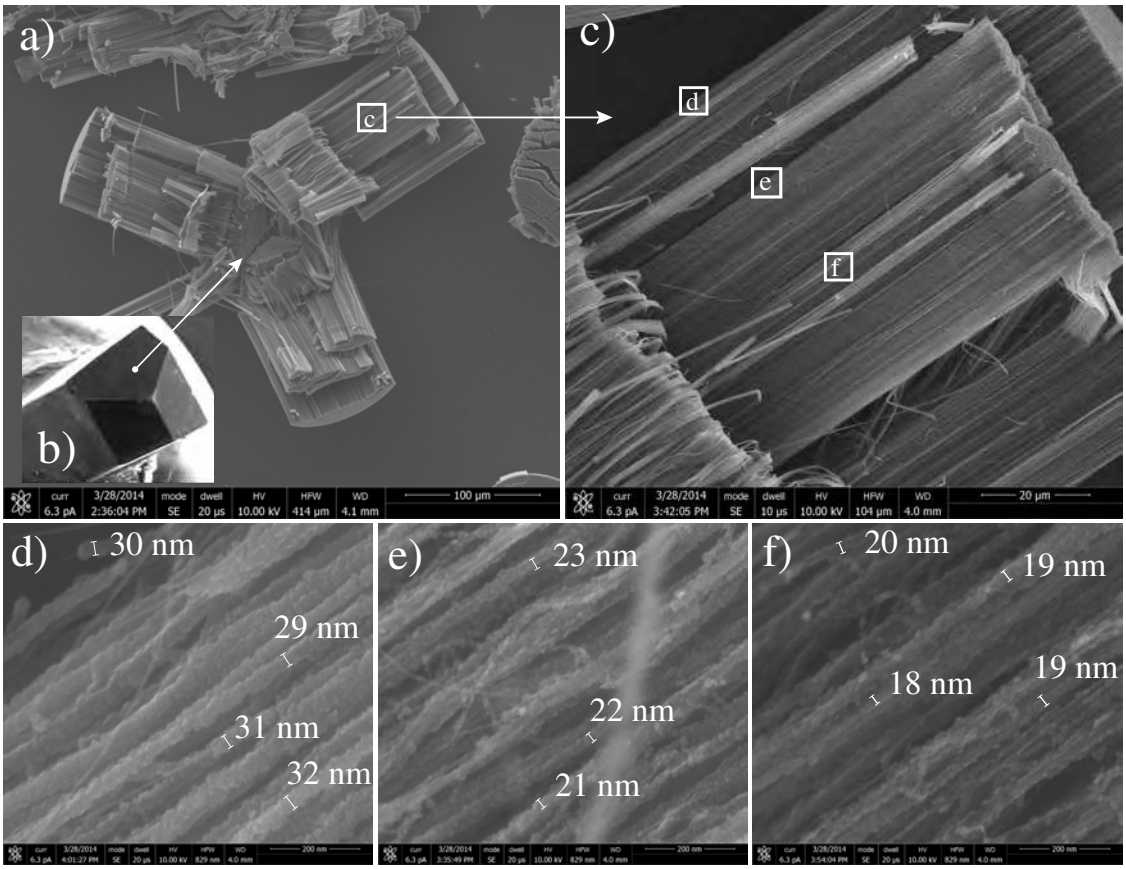

FIG. S3: (a) CNT pillar (100 µm diameter) with 10.5 nm a-SiC coating, cleaved with (b) a Berkovich nanoindentation tip. (c) Location used for investigation of the coating penetration depth. (d) Coating thickness of CNTs near the outer surface of the pillar. (e) Coating thickness at 20 µm distance from the surface. (f) Coating thickness at 40 µm distance from the surface.

3. Correlation between coating thickness and porosity

The density of the uncoated CNT array is about $n = 10^{10}\ tubes/cm^2$. Other researchers have reported similar densities in the order of 10^{10} to $10^{11}\ tubes/cm^2$ [4, 9, 51]. It should be noted that the density is very difficult to determine accurately and it is a very rough estimation. Fig. S4 shows that the average CNT diameter D_{cnt} is about 9 nm. Calculating the cross-sectional area of a single CNT using,

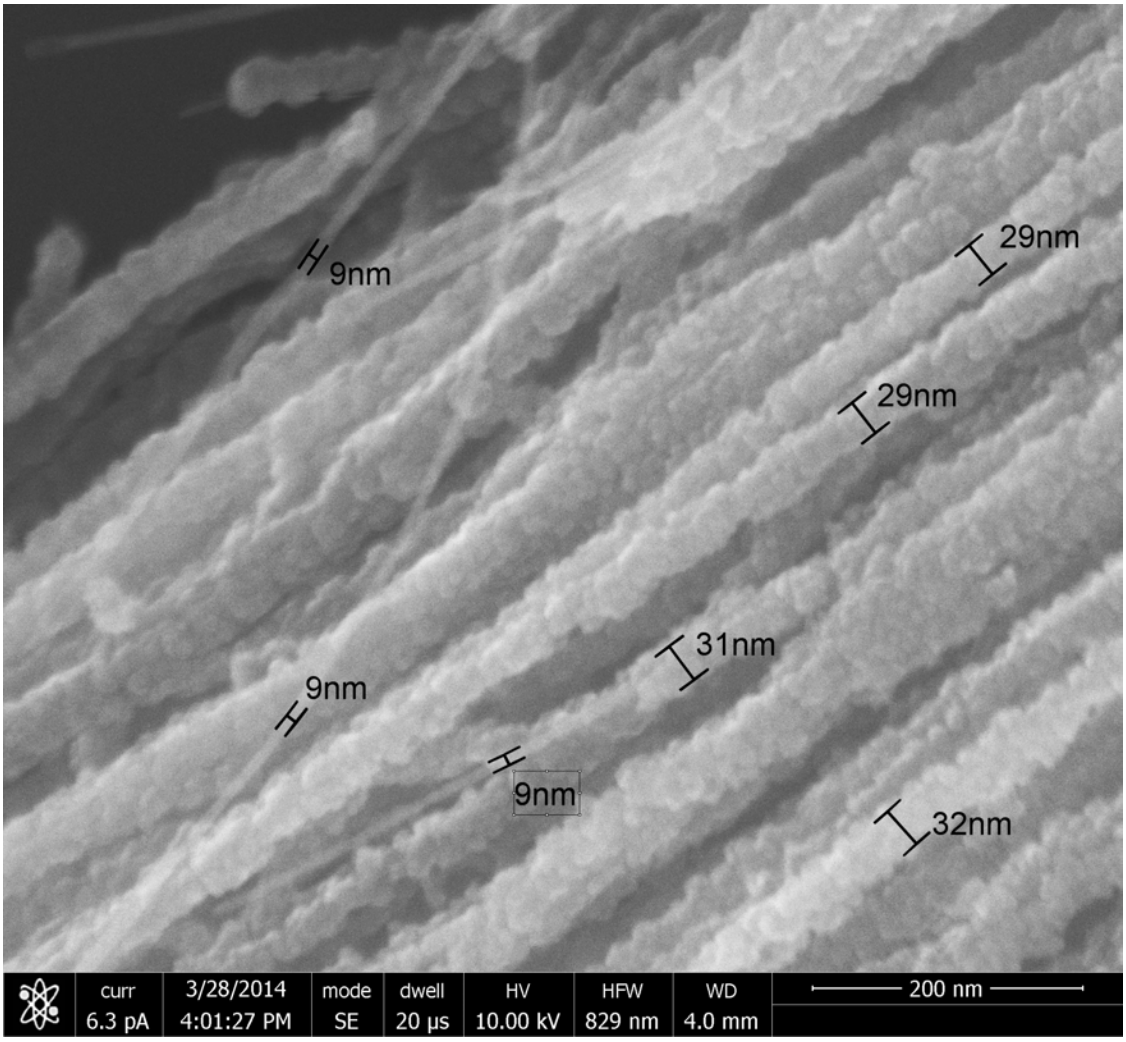

FIG. S4: Surface of a broken CNT pillar with a 10.5 nm thick conformal a-SiC coating, showing CNTs sticking out of the broken matrix.

$$A = \frac{\pi}{4}(D_{cnt} + 2t_{SiC})^2, \tag{A1}$$

we can determine the porosity as a function of the coating thickness, see Tab. S1. The measured properties of the a-SiC coated CNT pillars is just a fraction of the intrinsic properties of SiC due to the high porosity. The intrinsic SiC Youngs modulus ranges from 200 to 544 GPa, while the hardness ranges from 20 to 50 GPa [37, 39, 52–54]. Since the corrected material properties are strongly dependent on the porosity, and since the porosity is difficult to determine accurately, we think that the corrected bulk modulus can be inaccurate. A more useful property for engineering purposes, may be the measured effective Young's

TABLE S1: Pillar surface porosity and properties as function of the coating thickness.

Coating thickness $t_{SiC}(nm)$:	0	5.6	10.5	21.4
Porosity $p(\%)$:	99.4	96.8	92.9	78.9

modulus of the coated CNT arrays which we reported in the article in Fig. S7.

4. Raman spectroscopy

To determine the quality of the CNTs and the effects of a-SiC deposition we perform a Raman characterization using a Renishaw inVia system with a 514 nm wavelength Ar+ laser. Fig. S5 shows the Raman spectrum of the CNT arrays before and after a-SiC deposition. All curves are normalized towards the (G) peak amplitude and vertically offset.

Deposition of a-SiC directly on an oxidized Si substrate in curve (a) in Fig. S5, shows a sharp feature at 520 cm^{-1} and a smaller feature around 970 cm^{-1} which originate from the crystalline Si substrate. The weak bump near 1475 cm^{-1} can be connected to the presence of unprocessed acetylene used in the a-SiC deposition [55]. Fig. S5 curve (b) shows the Raman spectrum intensity of the as-grown CNT array, the peaks near 1580 cm^{-1} and 1350 cm^{-1} in the first order region correspond with the graphite (G) and disordered graphite (D) modes of the CNTs [51, 56–58]. The (G) peak has convolved with a shoulder peak at 1620 cm^{-1}, which is known as the (D') peak and is associated with graphite crystals and graphene edges which was fitted to a Gaussian curve. The intensity of the disordered graphite peak refers to the amount of micro crystalline graphite present inside the tube. The ratio I_G/I_D of the intensity peaks can be used to evaluate the quality of the CNTs, a higher ratio indicates a better quality. Curves (c), (d) and (e) are CNTs coated with a-SiC with an increasing film thickness. The location and amplitude of the deconvolved peaks were determined from fitted Lorentzian curves at 1350 and 1580 cm^{-1} and Gaussian curves at 1475 and 1620 cm^{-1}.

5. Nanoindentation measurements

The effects of a-SiC coatings on the mechanical response of CNT pillars is characterized using nanoindentation with an Agilent MTS Nanoindenter XP G200. Uniaxial compression of the CNT pillars was achieved by using a 150 µm diameter custom made flat-punch diamond

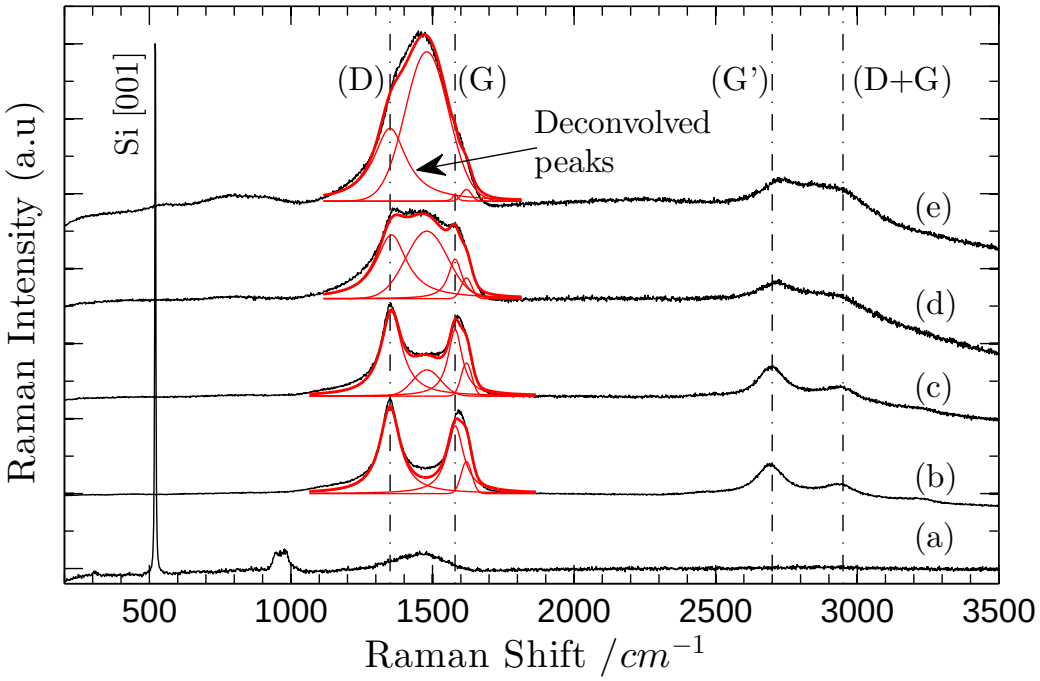

FIG. S5: Raman spectra intensity measurement with a 514 nm wavelength Ar+ laser normalized with respect to the graphite (G) mode. (a) Silicon substrate with 21.4 nm a-SiC. (b) As-grown CNT array. (c,d,e) CNT arrays with 5.6 nm, 10.5 nm, 21.4 nm and 52.0 nm a-SiC coating respectively.

indenter tip. A schematic illustration is shown in Fig. S6a. The pillars were compressed until failure occurs in the form of buckling or fracture, then unloading is initiated. The tested pillars have an average height of about (100 ± 2) µm and diameters ranging from (10 ± 1) µm to (150 ± 1) µm, see Fig. 1a. The coated samples were prepared with respectively, 5.6 nm, 10.5 nm, 21.4 nm and 52.0 nm thin, conformal coatings of a-SiC using LPCVD.

The flat surface of the tip allows for accurate detection of the CNT pillar surface and keeps a uniform contact area during compression [48]. For each test we detect the surface on a neighbouring pillar to avoid affecting the pillar on which measurements are performed. Force, displacement and stiffness data were acquired using the continuous stiffness measurement (CSM) technique. The main advantages of this technique are the continuous measurement of contact stiffness S_m as a function of depth δ, this eliminates the need for unloading cycles. The method relies on applying a small harmonic load with frequency ω on the nominal load. The CSM settings used are: 2 nm amplitude, 45 Hz frequency, sensitive 100 N m^{-1} surface detection and a strain rate of 0.01 s^{-1}. The measured contact stiffness S_m has been corrected

for S_f the indenter frame stiffness, S_t the diamond tip stiffness and S_s the substrate stiffness by modelling the entire system as springs in series, see Fig. S6b, and applying Eq. (A2) which gives S_p the pillar stiffness,

$$S_p = \frac{1}{1/S_m - 1/S_f - 1/S_t - 1/S_s}. \tag{A2}$$

The relationship between E the Young's modulus and S the contact stiffness is often given by *Sneddon's* relationship [59], see Eq. (A3) in this paper. However, this equation is more accurate when an elastic half space is compressed with a rigid flat-cylindrical punch. In this case the stresses are not uniform. In our case where relatively compliant pillars are compressed, the assumption of uniaxial compression and uniform stress becomes more accurate for the pillar, while *Sneddon's* relationship is more suitable for the substrate and tip. The stiffness of the silicon substrate and the diamond tip are therefore modelled as an elastic half-space which is being compressed with a flat spherical cylinder see Fig. S6b. The substrate and tip stiffnesses are directly proportional to pillar diameter and Young's modulus, see Eq. (A3). In the computation of S_s and S_t (Eq. (A3a) and Eq. (A3b)), we use $E_s = 130$ GPa and $v_s = 0.28$ for the Young's modulus and Poisson's ratio of the silicon substrate and $E_t = 1.2$ TPa and $v_t = 0.2$ for the diamond tip. The frame stiffness S_f, is a calibrated property and remains constant regardless of pillar diameter. The contact area $A = \pi D^2/4$, between the tip and the pillar is in our case defined by D the pillar diameter. The real surface contact area is lower and defined by the occupation fraction of the CNTs inside the array as well as the roughness of the pillar surface [9]. To simplify the computation of the material properties we assume constant contact area during compression and calculate the effective properties from the measured data.

$$S_s = \frac{2E_s}{1 - v_s^2}\sqrt{\frac{A}{\pi}} = \frac{E_s D}{1 - v_s^2} \tag{A3a}$$

$$S_t = \frac{2E_t}{1 - v_t^2}\sqrt{\frac{A}{\pi}} = \frac{E_t D}{1 - v_t^2} \tag{A3b}$$

After substitution of Eq. (A3a) and Eq. (A3b) for S_s and S_t into Eq. (A2) and solving for S_p the stiffness of the CNT pillars, we can compute the Young's modulus of the pillar using Eq. (A4). When S_p the sample stiffness approaches the stiffness of the measurement setup the corrections to S_m the measured stiffness become more significant, this occurs for large

diameter pillars with thick coatings. Henceforth we have taken the maximum measured pillar stiffness to perform a sensitivity analysis. The maximum corrections are 1%, 4%, 15% and 30% for uncoated and coated 100 μm diameter pillars with film thickness of 5.6 nm, 10.5 nm, 21.4 nm and 52.0 nm , respectively.

$$E_p = \frac{4S_p L}{\pi D^2}. \tag{A4}$$

Engineering stress σ and strain ϵ are computed from F the measured nanoindentation load, δ the tip displacement, L the undeformed pillar height and D the pillar diameter,

$$\sigma = \frac{F}{\pi D^2/4}, \quad \epsilon = \frac{\delta}{L} \tag{A5}$$

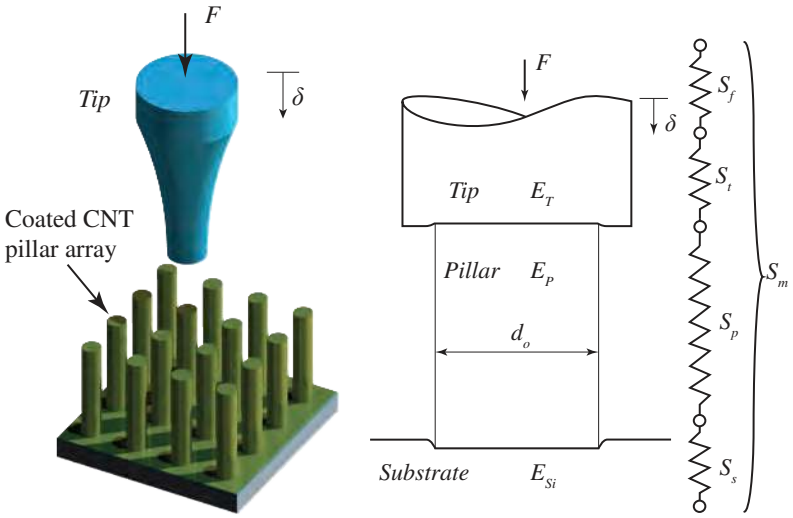

FIG. S6: Schematic illustration of (a) the flat-tip nanoindentation procedure, (b) the contact mechanics between indenter tip, pillar and substrate together with an equivalent spring model.

The effects of thin conformal a-SiC coatings on E the Young's modulus of CNT pillars are shown in Fig. S7. The results are discussed in II C. The pillar stiffness was measured using the continues stiffness measurement (CSM) mode of the nanoindenter and the respective Young's moduli is calculated using Eq. (A4).

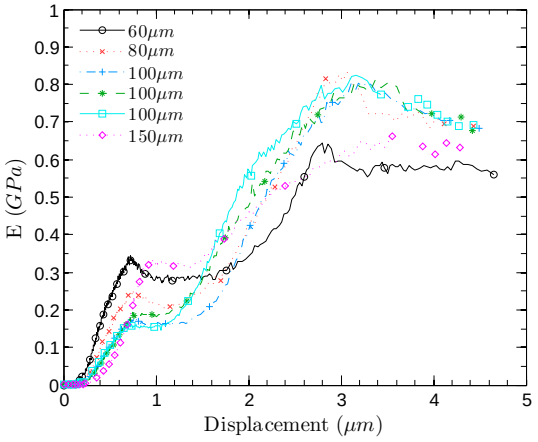

(a) As grown CNT pillars.

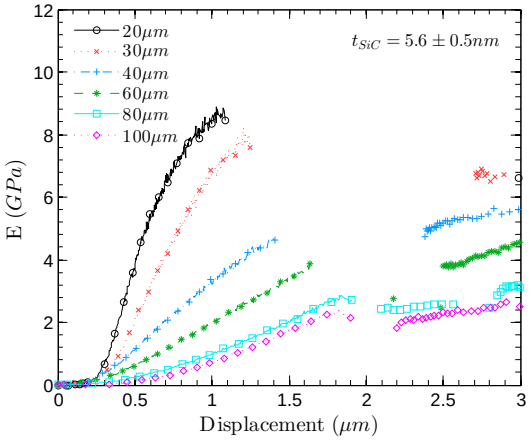

(b) with a 5.6 nm thick SiC coating.

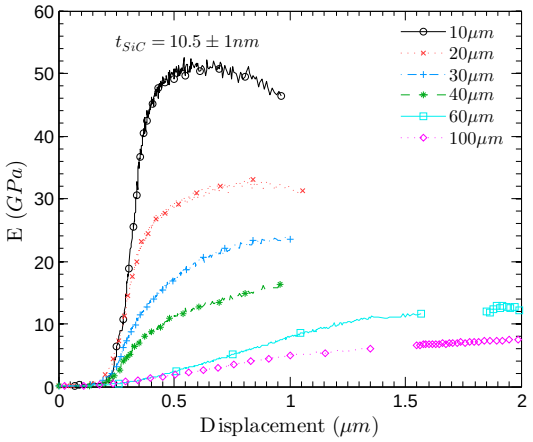

(c) with a 10.5 nm thick SiC coating.

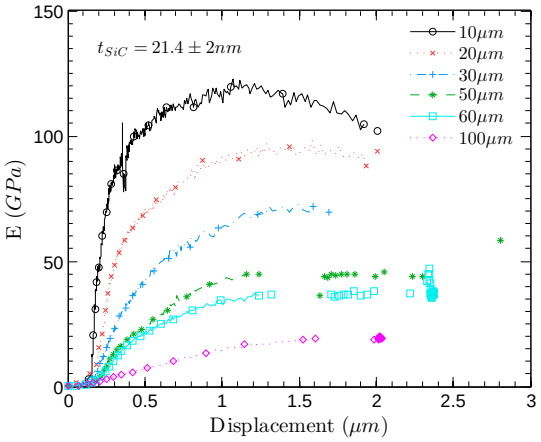

(d) with a 21.4 nm thick SiC coating.

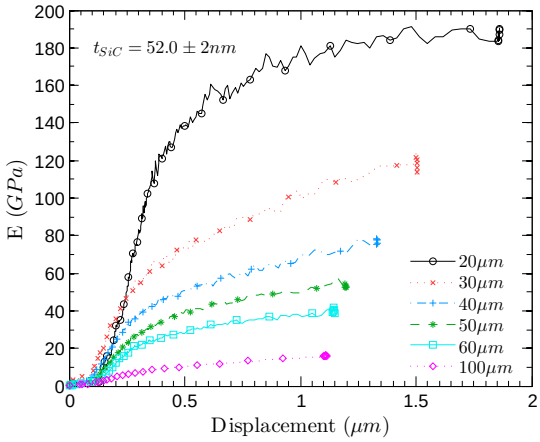

(e) with a 52.0 nm thick SiC coating.

FIG. S7: Effective Young's modulus of coated and uncoated CNT pillars with diameters ranging from 10 to 150 μm as a function of displacement.

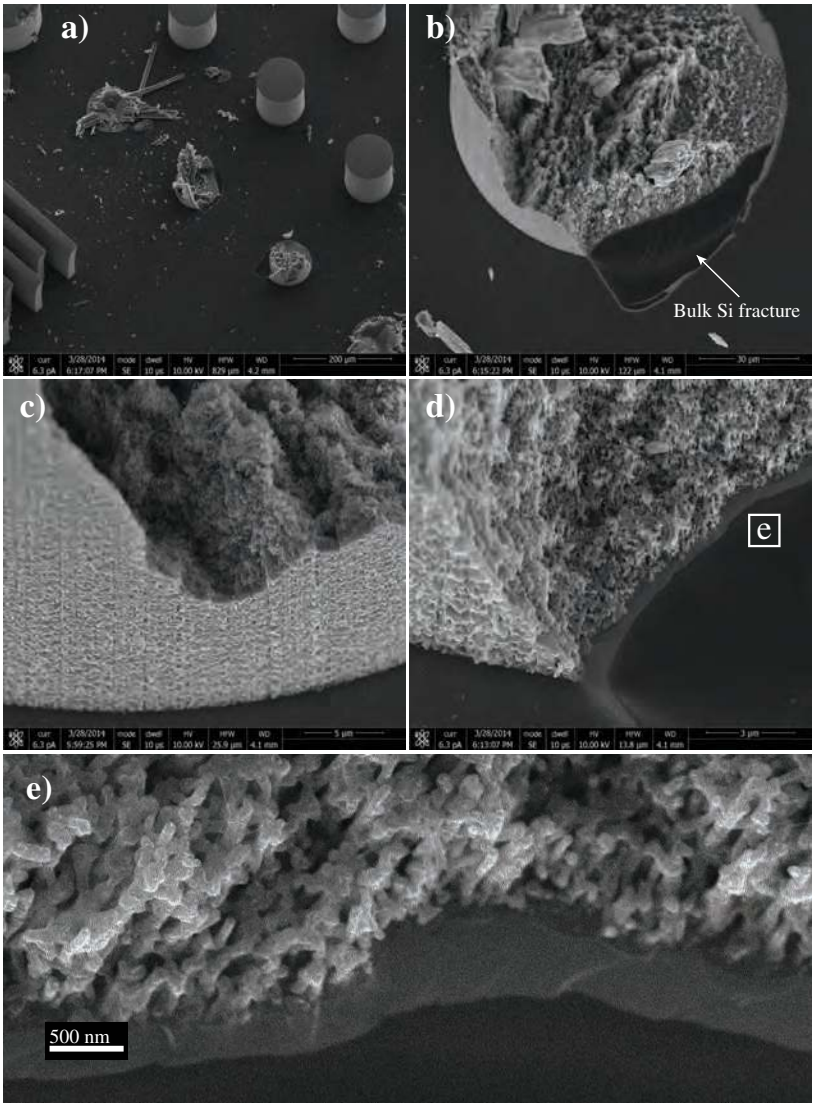

FIG. S8: Compressive failure of pillars coated with 52.0 nm a-SiC. The pillars could only be broken with a Berkovich nanoindentation tip.

[1] Y. Hayamizu, T. Yamada, K. Mizuno, R. C. Davis, D. N. Futaba, M. Yumura, K. Hata, Integrated three-dimensional microelectromechanical devices from processable carbon nanotube wafers, Nat Nano 3 (5) (2008) 289–294, 10.1038/nnano.2008.98.

[2] M. De Volder, S. H. Tawfick, S. J. Park, D. Copic, Z. Zhao, W. Lu, A. J. Hart, Diverse 3d microarchitectures made by capillary forming of carbon nanotubes, Advanced Materials 22 (39) (2010) 4384–4389.

[3] K. Fu, O. Yildiz, H. Bhanushali, Y. Wang, K. Stano, L. Xue, X. Zhang, P. D. Bradford, Aligned carbon nanotube-silicon sheets: A novel nano-architecture for flexible lithium ion battery electrodes, Advanced Materials 25 (36) (2013) 5109–5114.

[4] S. Tawfick, M. De Volder, A. J. Hart, Structurally programmed capillary folding of carbon nanotube assemblies, Langmuir 27 (10) (2011) 6389–6394.

[5] S. B. Hutchens, L. J. Hall, J. R. Greer, In situ mechanical testing reveals periodic buckle nucleation and propagation in carbon nanotube bundles, Advanced Functional Materials 20 (14) (2010) 2338–2346.

[6] M. F. L. De Volder, S. H. Tawfick, R. H. Baughman, A. J. Hart, Carbon nanotubes: Present and future commercial applications, Science 339 (6119) (2013) 535–539.

[7] K. H. Kim, Y. Oh, M. F. Islam, Graphene coating makes carbon nanotube aerogels superelastic and resistant to fatigue, Nat Nano 7 (9) (2012) 562–566, 10.1038/nnano.2012.118.

[8] Q. Tang, Z. Zhou, Z. Chen, Graphene-related nanomaterials: tuning properties by functionalization, Nanoscale 5 (11) (2013) 4541–4583.

[9] M. R. Maschmann, G. J. Ehlert, S. J. Park, D. Mollenhauer, B. Maruyama, A. J. Hart, J. W. Baur, Visualizing strain evolution and coordinated buckling within cnt arrays by in situ digital image correlation, Advanced Functional Materials 22 (22) (2012) 4686–4695.

[10] V. P. Veedu, A. Cao, X. Li, K. Ma, C. Soldano, S. Kar, P. M. Ajayan, M. N. Ghasemi-Nejhad, Multifunctional composites using reinforced laminae with carbon-nanotube forests, Nat Mater 5 (6) (2006) 457–462, 10.1038/nmat1650.

[11] A. Cao, P. L. Dickrell, W. G. Sawyer, M. N. Ghasemi-Nejhad, P. M. Ajayan, Supercompressible foamlike carbon nanotube films, Science 310 (5752) (2005) 1307–1310.

[12] A. Cao, V. P. Veedu, X. Li, Z. Yao, M. N. Ghasemi-Nejhad, P. M. Ajayan, Multifunctional brushes made from carbon nanotubes, Nat Mater 4 (7) (2005) 540–545, 10.1038/nmat1415.

[13] P. D. Bradford, X. Wang, H. Zhao, Y. T. Zhu, Tuning the compressive mechanical properties of carbon nanotube foam, Carbon 49 (8) (2011) 2834–2841.

[14] S. Vollebregt, F. D. Tichelaar, H. Schellevis, C. I. M. Beenakker, R. Ishihara, Carbon nanotube vertical interconnects fabricated at temperatures as low as 350 c, Carbon (0).

[15] L. Zhengchun, L. Ci, S. Kar, P. M. Ajayan, L. Jian-Qiang, Fabrication and electrical characterization of densified carbon nanotube micropillars for ic interconnection, Nanotechnology, IEEE Transactions on 8 (2) (2009) 196–203.

[16] A. Naeemi, J. D. Meindl, Carbon nanotube interconnects, Annual Review of Materials Research 39 (1) (2009) 255–275.

[17] Y.-C. Tseng, P. Xuan, A. Javey, R. Malloy, Q. Wang, J. Bokor, H. Dai, Monolithic integration of carbon nanotube devices with silicon mos technology, Nano Letters 4 (1) (2003) 123–127.

[18] A. M. Saleem, J. Berg, V. Desmaris, M. S. Kabir, Nanoimprint lithography using vertically aligned carbon nanostructures as stamps, Nanotechnology 20 (37) (2009) 375302.

[19] J. Wang, G. Min, Z. Song, X. Ni, W. Zhou, J. Zhan, Y. Zhang, J. Zhang, L. Shi, Solvent-infiltration imprint lithography: a novel method to prepare large area poly(3-hexylthiophene) micro/nano-patterns, Journal of Materials Chemistry 22 (39) (2012) 21154–21158.

[20] Z. Nie, E. Kumacheva, Patterning surfaces with functional polymers, Nat Mater 7 (4) (2008) 277–290, 10.1038/nmat2109.

[21] X. F. Zeng, S. C. Shei, S. J. Chang, Gan-based leds with nano-patterns by contact-transferred and mask-embedded lithography and cl2/n2 plasma etching, ECS Solid State Letters 1 (6) (2012) R27–R30.

[22] C. Robert, A. C. Baratunde, F. Timothy, X. Xianfan, G. Ken, G. Samuel, A metallization and bonding approach for high performance carbon nanotube thermal interface materials, Nanotechnology 21 (44) (2010) 445705.

[23] J. Xu, T. S. Fisher, Enhancement of thermal interface materials with carbon nanotube arrays, International Journal of Heat and Mass Transfer 49 (910) (2006) 1658–1666.

[24] A. A. Balandin, Thermal properties of graphene and nanostructured carbon materials, Nat Mater 10 (8) (2011) 569–581, 10.1038/nmat3064.

[25] X. Tian, M. E. Itkis, E. B. Bekyarova, R. C. Haddon, Anisotropic thermal and electrical properties of thin thermal interface layers of graphite nanoplatelet-based composites, Sci. Rep. 3.

[26] C. L. Pint, N. W. Nicholas, S. Xu, Z. Sun, J. M. Tour, H. K. Schmidt, R. G. Gordon, R. H. Hauge, Three dimensional solid-state supercapacitors from aligned single-walled carbon nanotube array templates, Carbon 49 (14) (2011) 4890–4897.

[27] G. Fiorentino, S. Vollebregt, F. D. Tichelaar, R. Ishihara, P. M. Sarro, 3d solid-state supercapacitors obtained by ald coating of high-density carbon nanotubes bundles, in: Micro Electro Mechanical Systems (MEMS), 2014 IEEE 27th International Conference on, pp. 342–345.

[28] D. N. Hutchison, N. B. Morrill, Q. Aten, B. W. Turner, B. D. Jensen, L. L. Howell, R. R. Van-

fleet, R. C. Davis, Carbon nanotubes as a framework for high-aspect-ratio mems fabrication, Microelectromechanical Systems, Journal of 19 (1) (2010) 75–82.

[29] J. A. Weldon, B. Aleman, A. Sussman, W. Gannett, A. K. Zettl, Sustained mechanical self-oscillations in carbon nanotubes, Nano Letters.

[30] P. M. Sousa, M. Gutierrez, E. Mendoza, A. Llobera, V. Chu, J. P. Conde, Microelectromechanical resonators based on an all polymer/carbon nanotube composite structural material, Applied Physics Letters 99 (4) (2011) 044104–3.

[31] V. Ivanov, J. B. Nagy, P. Lambin, A. Lucas, X. B. Zhang, X. F. Zhang, D. Bernaerts, G. Van Tendeloo, S. Amelinckx, J. Van Landuyt, The study of carbon nanotubules produced by catalytic method, Chemical Physics Letters 223 (4) (1994) 329–335.

[32] S. Fan, M. G. Chapline, N. R. Franklin, T. W. Tombler, A. M. Cassell, H. Dai, Self-oriented regular arrays of carbon nanotubes and their field emission properties, Science 283 (5401) (1999) 512–514.

[33] T. Wang, K. Jeppson, J. Liu, Dry densification of carbon nanotube bundles, Carbon 48 (13) (2010) 3795–3801.

[34] A. Misra, J. R. Greer, C. Daraio, Strain rate effects in the mechanical response of polymer-anchored carbon nanotube foams, Advanced Materials 21 (3) (2009) 334–338.

[35] A. Kis, G. Csanyi, J. P. Salvetat, T.-N. Lee, E. Couteau, A. J. Kulik, W. Benoit, J. Brugger, L. Forro, Reinforcement of single-walled carbon nanotube bundles by intertube bridging, Nat Mater 3 (3) (2004) 153–157, 10.1038/nmat1076.

[36] R. L. D. Whitby, W. K. Hsu, Y. Q. Zhu, H. W. Kroto, D. R. M. Walton, Novel nanoscale architectures: coated nanotubes and other nanowires, Philosophical Transactions of the Royal Society of London. Series A: Mathematical, Physical and Engineering Sciences 362 (1823) (2004) 2127–2142.

[37] Y. Gogotsi, S. Welz, D. A. Ersoy, M. J. McNallan, Conversion of silicon carbide to crystalline diamond-structured carbon at ambient pressure, Nature 411 (6835) (2001) 283–287, 10.1038/35077031.

[38] B. Morana, G. Pandraud, J. F. Creemer, P. M. Sarro, Characterization of lpcvd amorphous silicon carbide (a-sic) as material for electron transparent windows, Materials Chemistry and Physics 139 (23) (2013) 654–662.

[39] S. M. Spearing, Materials issues in microelectromechanical systems (mems), Acta Materialia

48 (1) (2000) 179–196.

[40] T. Taguchi, A. K. M. F. Kibria, S. Shamoto, Morphology change of multi-walled carbon nanotubes with sic coating by electron irradiation, Journal of Physics: Conference Series 417 (1) (2013) 012037.

[41] R. Gupta, R. Mishra, K. Mukhopadhyay, R. Tiwari, A. Ranjan, A. Saxena, A new technique for coating silicon carbide onto carbon nanotubes using a polycarbosilane precursor, Silicon 1 (2) (2009) 125–129.

[42] Z. Gu, Y. Yang, K. Li, X. Tao, G. Eres, J. Y. Howe, L. Zhang, X. Li, Z. Pan, Aligned carbon nanotube-reinforced silicon carbide composites produced by chemical vapor infiltration, Carbon 49 (7) (2011) 2475–2482.

[43] Y. Morisada, Y. Miyamoto, Y. Takaura, K. Hirota, N. Tamari, Mechanical properties of sic composites incorporating sic-coated multi-walled carbon nanotubes, International Journal of Refractory Metals and Hard Materials 25 (4) (2007) 322–327.

[44] J. Greer, D. Jang, X. W. Gu, Exploring deformation mechanisms in nanostructured materials, JOM 64 (10) (2012) 1241–1252.

[45] T. Y. Lo, H. Z. Cui, H. C. Leung, The effect of fiber density on strength capacity of bamboo, Materials Letters 58 (21) (2004) 2595–2598.

[46] K. F. Chung, W. K. Yu, Mechanical properties of structural bamboo for bamboo scaffoldings, Engineering Structures 24 (4) (2002) 429–442.

[47] S. Pathak, E. J. Lim, P. Pour Shahid Saeed Abadi, S. Graham, B. A. Cola, J. R. Greer, Higher recovery and better energy dissipation at faster strain rates in carbon nanotube bundles: An in-situ study, ACS Nano 6 (3) (2012) 2189–2197.

[48] M. R. Maschmann, Q. Zhang, F. Du, L. Dai, J. Baur, Length dependent foam-like mechanical response of axially indented vertically oriented carbon nanotube arrays, Carbon 49 (2) (2011) 386–397.

[49] C. San Marchi, A. Mortensen, Deformation of open-cell aluminum foam, Acta Materialia 49 (19) (2001) 3959–3969.

[50] P. B. Amama, C. L. Pint, S. M. Kim, L. McJilton, K. G. Eyink, E. A. Stach, R. H. Hauge, B. Maruyama, Influence of alumina type on the evolution and activity of alumina-supported fe catalysts in single-walled carbon nanotube carpet growth, ACS Nano 4 (2) (2010) 895–904.

[51] S. Vollebregt, R. Ishihara, F. D. Tichelaar, Y. Hou, C. I. M. Beenakker, Influence of the

growth temperature on the first and second-order raman band ratios and widths of carbon nanotubes and fibers, Carbon 50 (10) (2012) 3542–3554.

[52] S. Maruthoor, A. Ajayakumar, T. Fuchs, O. Jakovlev, H. Reinecke, J. Wilde, Mechanical characterization of polycrystalline and amorphous silicon carbide thin films using bulge test, Microelectromechanical Systems, Journal of 22 (1) (2013) 140–146.

[53] J. M. Grow, R. A. Levy, M. Bhaskaran, H. J. Boeglin, R. Shalvoy, Low pressure chemical vapor deposition of silicon carbide from ditertiarybutylsilane, Journal of The Electrochemical Society 140 (10) (1993) 3001–3007.

[54] M. A. El Khakani, M. Chaker, A. Jean, S. Boily, J. C. Kieffer, M. E. O'Hern, M. F. Ravet, F. Rousseaux, Hardness and young's modulus of amorphous a-sic thin films determined by nanoindentation and bulge tests, Journal of Materials Research 9 (01) (1994) 96–103.

[55] A. C. Ferrari, J. Robertson, Raman spectroscopy of amorphous, nanostructured, diamondlike carbon, and nanodiamond, Philosophical Transactions of the Royal Society of London. Series A: Mathematical, Physical and Engineering Sciences 362 (1824) (2004) 2477–2512.

[56] J. Schwan, S. Ulrich, V. Batori, H. Ehrhardt, S. R. P. Silva, Raman spectroscopy on amorphous carbon films, Journal of Applied Physics 80 (1) (1996) 440–447.

[57] J. Yang, Y. Yang, S. W. Waltermire, T. Gutu, A. A. Zinn, T. T. Xu, Y. Chen, D. Li, Measurement of the intrinsic thermal conductivity of a multiwalled carbon nanotube and its contact thermal resistance with the substrate, Small 7 (16) (2011) 2334–2340.

[58] A. C. Ferrari, J. Robertson, Interpretation of raman spectra of disordered and amorphous carbon, Physical Review B 61 (20) (2000) 14095–14107, pRB.

[59] I. N. Sneddon, The relation between load and penetration in the axisymmetric boussinesq problem for a punch of arbitrary profile, International Journal of Engineering Science 3 (1) (1965) 47–57.